

Force Correlations in Disordered Magnets

Cathelijne ter Burg¹, Felipe Bohn², Gianfranco Durin³, Rubem Luis Sommer⁴, Kay Jörg Wiese¹

¹ *Laboratoire de Physique de l'École Normale Supérieure, ENS, Université PSL, CNRS, Sorbonne Université, Université Paris-Diderot, Sorbonne Paris Cité, 24 rue Lhomond, 75005 Paris, France*

² *Departamento de Física, Universidade Federal do Rio Grande do Norte, 59078-900 Natal, RN, Brazil*

³ *Istituto Nazionale di Ricerca Metrologica, strada delle Cacce 91, Torino, Italy*

⁴ *Centro Brasileiro de Pesquisas Físicas, Rua Dr. Xavier Sigaud 150, Urca, 22290-180 Rio de Janeiro, RJ, Brazil*

We present a *proof of principle* for the validity of the functional renormalization group, by measuring the force correlations in Barkhausen-noise experiments. Our samples are soft ferromagnets in two distinct universality classes, differing in the range of spin interactions, and the effects of eddy currents. We show that the force correlations have a universal form predicted by the functional renormalization group, distinct for short-range and long-range elasticity, and mostly independent of eddy currents. In all cases correlations grow linearly at small distances, as in mean-field models, but in contrast to the latter are bounded at large distances. As a consequence, avalanches are anti-correlated. We derive bounds for these anti-correlations, which are saturated in the experiments, showing that the multiple domain walls in our samples effectively behave as a single wall.

Each theory of disordered systems relies on specific assumptions, and often their validity is checked only for standard observables, such as the roughness exponent. Measuring its central ingredients would be a much more stringent test to discriminate between them. Two general theories have been proposed: the Gaussian variational ansatz invoking replica-symmetry breaking [1–3], which is exact for fully connected models [4, 5], and the functional renormalization group (FRG) for short-ranged elastic systems [6, 7], where the central ingredient is the effective force correlator. This correlator is the solution of a non-linear partial differential equation [6–8], and can experimentally be extracted from the center-of-mass fluctuations of the interface.

To prove the validity of the FRG for disordered systems, we analyse the domain-wall motion in soft magnets (the Barkhausen noise) [9], the oldest example of depinning and avalanche motion [8, 10–12]. Standard observables as the avalanche size, duration [13, 14] and shape [15–18] show the existence of two universality classes differing in the kind and range of domain-wall interactions [12, 14]: amorphous materials with short-range (SR) interactions and polycrystals with long-range (LR) interactions, consequence of strong dipolar effects. In 3D magnets, the latter is described by mean-field models pioneered in 1990 by Alessandro, Beatrice, Bertotti and Montorsi (ABBM) [19–21], where a domain wall is represented by a single degree of freedom, its centre of mass, a.k.a. *mean field* (MF). For the SR class, key observables as the avalanche-size exponent $\tau \simeq 1.27$ differ from their MF prediction $\tau_{\text{MF}} = 3/2$, while they are accounted for by field-theoretic models [22–24].

In view of the solid evidence for exponents, a central question is whether experiments can contradict the ABBM model in a key prediction for LR magnets. We show that this is the case for the force correlator acting on the domain wall, or equivalently the correlator of its centre of mass. To understand this, consider the equation of motion of a d -dimensional interface with SR interactions,

$$\eta \partial_t u(x, t) = \nabla^2 u(x, t) + m^2 [w - u(x, t)] + F(x, u(x, t)),$$

$$w = vt. \quad (1)$$

Here w is proportional to the external applied field, increased

very slowly, and m^2 , usually denoted k , is the *demagnetization factor* [12]. Averaging Eq. (1) over x , given w , we get $\eta \dot{u}_w = m^2 [w - u_w] + F_w$. Most of the time $\dot{u}_w = 0$, and the position and force correlations are

$$\hat{\Delta}_v(w - w') := \overline{[w - u_w][w' - u_{w'}]}^c \simeq \frac{1}{m^4} \overline{F_w F_{w'}}^c, \quad (2)$$

where the overbar designates a disorder average and c its connected part. In practice it is taken both over w and runs. $\hat{\Delta}_v$ depends on the driving velocity. Its zero-velocity limit

$$\hat{\Delta}(w) = \lim_{v \rightarrow 0} \hat{\Delta}_v(w), \quad (3)$$

is the central object of the FRG field theory [7, 8, 25–27].

In an experiment, it is impossible to take $v \rightarrow 0$. The effect of $v > 0$ is to round the cusp $|\hat{\Delta}'(0^+)| = \sigma$ (see Eq. (6)) in a boundary layer of size $\delta_w \sim v\tau$, where τ is the timescale set by the response function $R(t) \simeq \frac{1}{\tau} e^{-t/\tau}$ (see Fig. 2(c) for an example). Ref. [28] shows that

$$\hat{\Delta}_v(w) = \int_0^\infty dt \int_0^\infty dt' R(t) R(t') \hat{\Delta}(w - v(t - t')) \quad (4)$$

can be deconvoluted to reconstruct $\hat{\Delta}(w)$ from the measured $\hat{\Delta}_v(w)$ (see App. D). The result is

$$\hat{\Delta}(w) = \hat{\Delta}_v(w) + \tau^2 \hat{\Delta}_{\dot{u}}(w), \quad (5)$$

where $\hat{\Delta}_{\dot{u}}(w)$ is the auto-correlation function of the measured \dot{u}_w . This allows us to extract $\hat{\Delta}(w)$ by plotting the r.h.s. and finding τ that best eliminates the rounding close to $w = 0$. As shown below, Eq. (5) allows us to remove a boundary layer of size $\delta_w = v\tau$, but it creates a smaller one of size $\delta'_w = v\tau'$, see App. E.

The ABBM model assumes that forces F_w perform a random walk, and as a consequence

$$\frac{1}{m^4} \frac{1}{2} \overline{[F_w - F_{w'}]^2} = \hat{\Delta}(0) - \hat{\Delta}(w - w') \simeq \sigma |w - w'|. \quad (6)$$

Field theory [8, 30, 31] predicts $\hat{\Delta}(0) - \hat{\Delta}(w)$ to grow linearly as Eq. (6) for small w , and to saturate for large w , with

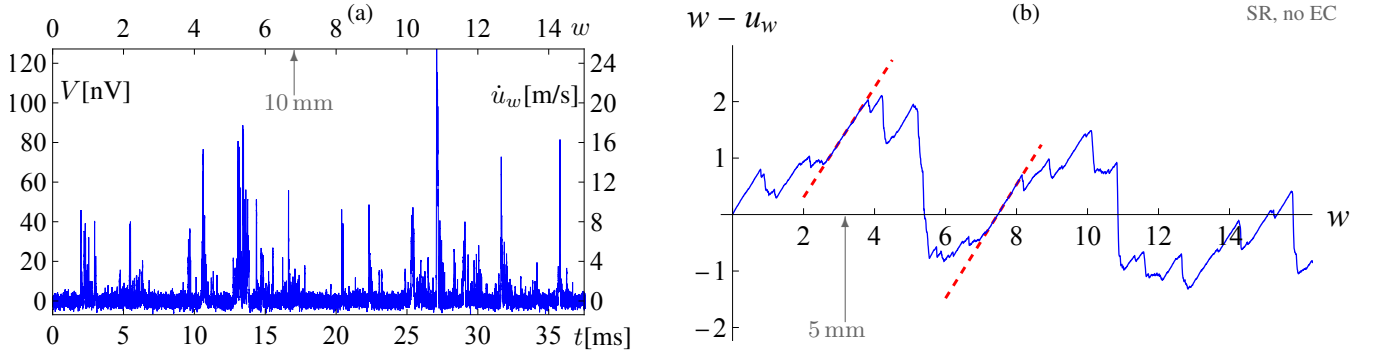


FIG. 1. Barkhausen noise in an amorphous FeSiB film (table I). **(a)** Voltage signal recorded in the experiment (left axis), and corresponding domain-wall velocity \dot{u}_w (right axis), as a function of time (bottom axis) and w (top axis). **(b)** The connected part of the interface position, $w - u_w$, obtained by integrating \dot{u}_w . $w = 1$ corresponds to $2.5 \text{ ms} \approx 1.5 \text{ mm}$. Physical units are indicated by grey arrows.

distinct shapes in SR and LR systems (see App. C). While this framework was tested in simulations [28, 32], and experiments on wetting [33] and RNA/DNA peeling [34], only with magnets we can consider two universality classes, and with a large statistics.

We analyze our experimental data as follows. We start from the Barkhausen-noise time series, proportional to the center-of-mass velocity \dot{u}_w (See Fig. 1(a)). The signal is characterized by bursts when the domain wall moves forward, and a vanishing signal when it is pinned i.e. at rest, combined with background noise (without noise $\dot{u}_w \geq 0$ [35]). This allows us to reconstruct the position of the center of mass u_w (see Eq. (2)), as depicted in Fig. 1(b). It is characterized by linearly increasing parts with slope 1, corresponding to an increasing magnetic field (i.e. w), followed by drops in $w - u_w$ when the wall moves forward. This allows us to reconstruct the unknown scale between \dot{u}_w and the voltage induced in the pickup coil, reducing the scales in the experiment to a single one (see App. B).

We analyse $\hat{\Delta}(w)$ in different materials, summarised in Table I. We also consider data where eddy currents (EC) play a noticeable effect [9, 12, 15, 16], an aspect experimentally tunable by varying the sample thickness [9, 15, 16]. Details on samples are given in App. A, and on the data analysis in App. F, including conversion of our units of w to physical space and time.

SR interactions without ECs. Our first sample is an amorphous 200-nm-thick FeSiB film. Fig. 2(a) shows that the raw data for $\hat{\Delta}(w)$ are rounded in a boundary layer of size $\delta_w \approx 0.6$, due to the finite driving velocity. To obtain $\hat{\Delta}(w)$,

we use Eq. (5) with $\tau = 0.17$. This reduces the boundary layer (non-straight part) from $\delta_w \approx 0.6$ to $\delta_w \approx 0.1$, allowing us to extrapolate to $w = 0$ (grey in Fig. 2(a,b)). The measured values for $\hat{\Delta}(0)$ and $\hat{\Delta}'(0^+)$ are then used to fix all scales in the theory predictions we wish to compare to on Fig. 2(b). These are from bottom to top (analytic expressions are in App. C): 1-loop FRG (relevant for $d = d_c$, i.e. LR elasticity), 2-loop FRG in $d = 2$ (relevant for SR elasticity) [30, 31], the $d = 0$ solution [28, 36] and an exponential, the latter, not realized in magnets, given as reference. The data agree best, and within error bars, with the 2-loop FRG prediction for $d = 2$. From Fig. 2(b) we extract a correlation length $\rho := \hat{\Delta}(0)/\hat{\Delta}'(0) \approx 3$. This agrees with the scale on which $\hat{\Delta}_u(w)$ decays to 0 (see Fig. 10(a) in App. G).

SR interactions with ECs. Our second sample with SR elasticity is an amorphous FeCoB ribbon where ECs are non-negligible. A range of different driving velocities is at our disposal. As ECs are more relevant as v increases, we focus on $v = 1, 2, 3$. There is additional (white) noise contributing to \dot{u} . After integration this contributes a linear function to $\hat{\Delta}(w)$, s.t.

$$\hat{\Delta}_v^{\text{raw}}(0) - \hat{\Delta}_v^{\text{raw}}(w) = \hat{\Delta}_v(0) - \hat{\Delta}_v(w) + \sigma_{\text{noise}}|w|, \quad (7)$$

necessitating to subtract a linear term $\sigma_{\text{noise}}|w|$ (see Fig. 8 in App. F2). Fig. 2(c) shows $\hat{\Delta}_v(w)$ after this subtraction. The inset zooms into the boundary layer with deconvolution by Eq. (5) in the same color code. Having data at different v allows us to test that

(i) the boundary layer scales linearly in v , i.e. $\delta_w \sim v\tau$.

(ii) $\hat{\Delta}_v(w)$ for $v = 1, 2, 3$ unfold to the same $\hat{\Delta}(w)$.

Both conditions are satisfied using $\tau = 0.025$. Comparison to the theory proceeds as before, and is shown in Fig. 2(d), combining $v = 1$ and $v = 2$ to improve the statistics. Although error bars are non-negligible, the data is in agreement with the predicted 2-loop result in $d = 2$, as for FeSiB with SR elasticity without ECs in Fig. 2(b). For $w > 0.7$ the data slightly deviate from the 2-loop result, albeit well within error bars. Either this is a statistical fluctuation, or due to ECs.

sample	interactions / eddy currents	correlation length ρ
amorphous FeSiB film	SR / no	$7.5 \text{ ms} \approx 495 \mu\text{m}$
amorphous FeCoB ribbon	SR / yes	$0.1 \text{ s} \approx 67.5 \mu\text{m}$
polycrystalline NiFe film	LR / no	$12.5 \text{ ms} \approx 500 \mu\text{m}$
polycrystalline FeSi ribbon	LR / yes	$35 \text{ ms} \approx 0.9695 \mu\text{m}$

TABLE I. Short-range (SR) and long-range (LR) samples, with and without eddy currents (ECs).

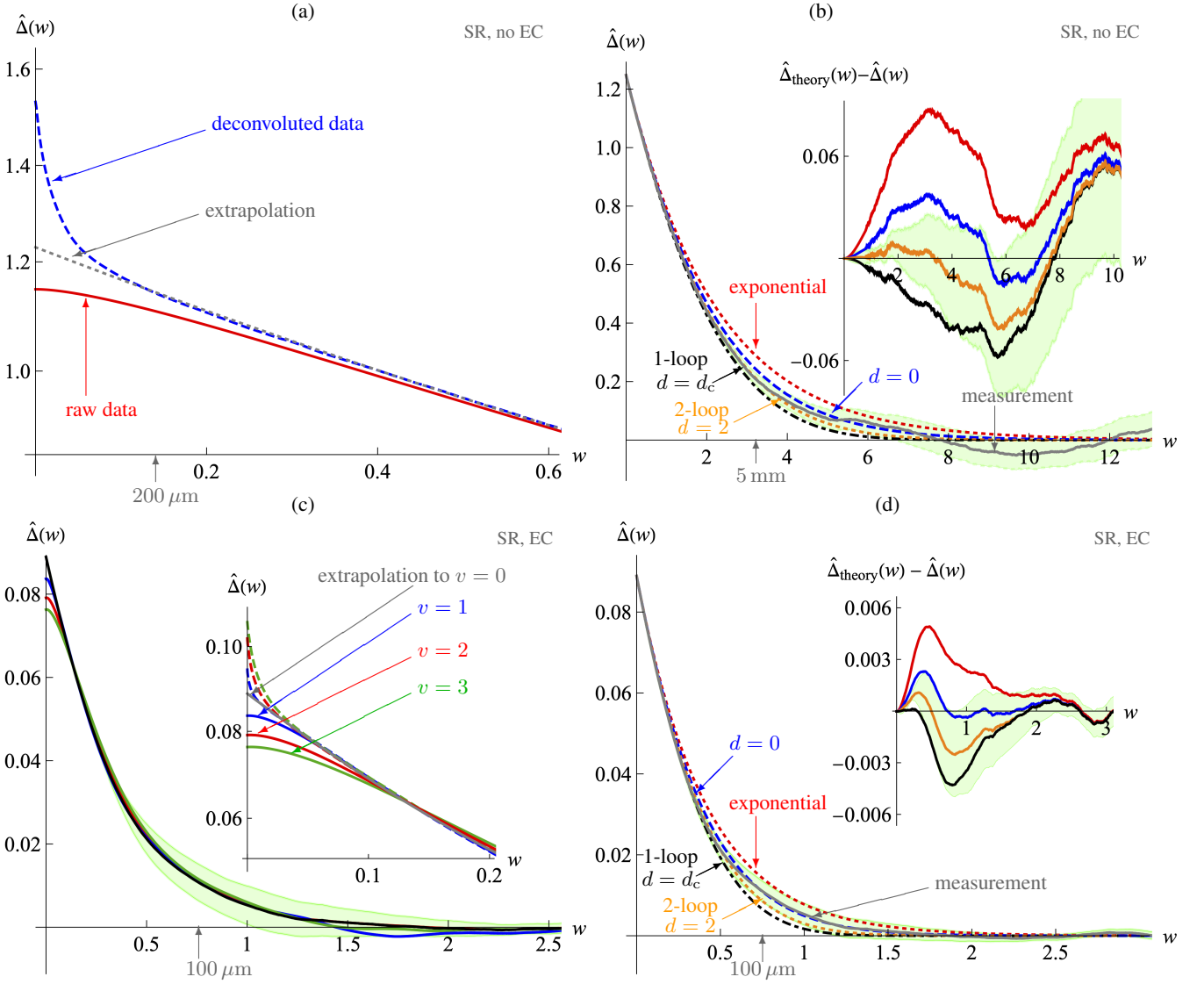


FIG. 2. **(a)** Construction of $\hat{\Delta}(w)$ for the FeSiB film (SR, no ECs). In red the raw data. In blue dashed, the result from Eq. (5) using $\tau = 0.17$. In dotted gray the extrapolation to $w = 0$. **(b)** Comparison of $\hat{\Delta}(w)$ using the dotted gray curve of (a), to theory candidates, fixing scales by $\hat{\Delta}(0)$ and $\hat{\Delta}'(0^+)$. The latter are from top to bottom: exponential (red, dotted), solution in $d = 0$ [28, 36] (blue, dashed), 2-loop FRG via Padé for $d = 2$ (orange, dotted), 1-loop FRG (black, dot-dashed). Error bars in green for $1\text{-}\sigma$ confidence intervals. The inset shows theory minus data in the same color code, favoring $d = 2$ FRG at two loops (with error bars for this curve only). **(c)** Check of deconvolution Eq. (5), for the FeCoB ribbon (SR, noticeable ECs), at different driving velocities v , using the same time scale $\tau = 0.025$; magnified in the inset. Apart from a small deviation for $v = 3$ they extrapolate to the same function. **(d)** Comparison of $\hat{\Delta}(w)$ from (c) to the theory, using the color code of Fig. (b). The data is consistent with 2-loop FRG in $d = 2$. $w = 1$ corresponds to $2.5 \text{ ms} \approx 1.5 \text{ mm}$ for (a)-(b), and to $0.2 \text{ s} \approx 135 \mu\text{m}$ for (c)-(d), see grey arrows.

LR interactions without ECs. LR elasticity arises in materials, here a polycrystalline 200-nm-thick NiFe film, due to strong dipolar interactions between parts of the domain wall. For long-range elasticity the upper critical dimension $d_c = 2$ coincides with the dimension of the wall. The common belief is that then MF theory, i.e. the ABBM model, is sufficient to describe the system. A glance at Fig. 3(a) shows that the experimental result is in contradiction to the prediction (6) of ABBM. While the latter holds at small w , at larger w the correlator $\hat{\Delta}(w)$ decays to zero. Field theory pre-

dicts [30, 31, 37, 38] that fluctuations are relevant at the upper critical dimension, and that $\hat{\Delta}(w)$ is given by 1-loop FRG. Fig. 3(a) shows that this is indeed the case.

LR interactions with ECs. Our fourth sample is a polycrystalline FeSi ribbon where the elasticity is LR and ECs are non-negligible. Fig. 3(b) shows a comparison of $\hat{\Delta}(w)$ to the four theory candidates. As for the NiFe film with LR elasticity and no ECs, the agreement is excellent with 1-loop FRG, and inconsistent with ABBM. We refer to App. F4 and Fig. 9 for details on the data analysis for this sample.

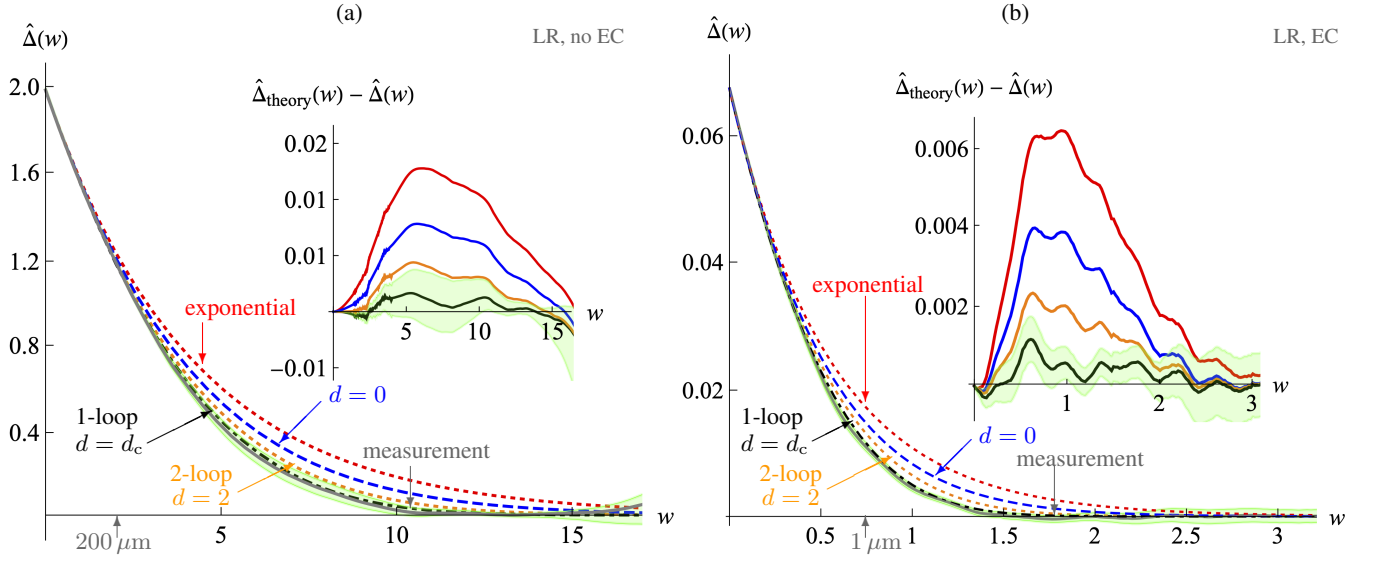


FIG. 3. The measured function $\hat{\Delta}(w)$ for our two LR samples: (a) a polycrystalline 200-nm-thick NiFe film (negligible ECs), and (b) a polycrystalline FeSi ribbon (with ECs). They agree with 1-loop FRG relevant here. $w = 1$ corresponds to $2.5 \text{ ms} \approx 100 \mu\text{m}$ for (a), and $50 \text{ ms} \approx 1.385 \mu\text{m}$ for (b), see grey arrows.

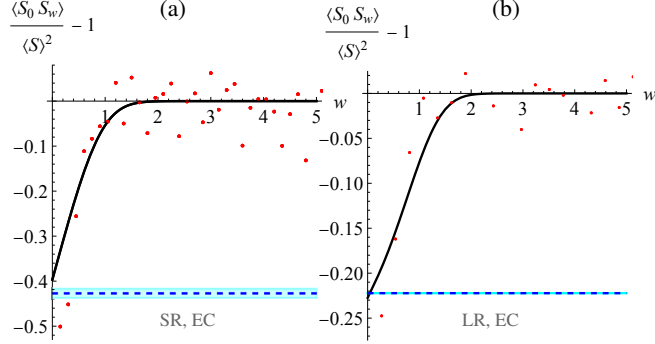


FIG. 4. Anticorrelation of avalanches as a function of w as defined in Eq. (8), for the two samples with ECs (red dots), (a) FeCoB with SR elasticity and (b) FeSi with LR elasticity. The solid line is the prediction $-\hat{\Delta}''(w)$ of Eq. (8) from the experiment. The dashed lines are bounds on the maximal reduction from the field-theory (9), with error bars in cyan. $w = 1$ corresponds to $200 \text{ ms} \approx 135 \mu\text{m}$ for (a) and $50 \text{ ms} \approx 1.385 \mu\text{m}$ for (b).

In experiments, force correlations are bounded, and do not grow indefinitely as in MF models such as ABBM [19–21], see Eq. (6). As a consequence (Ref. [8] section 4.20, or [39], Eq. (8)), avalanches are anti-correlated

$$\frac{\langle S_{w_1} S_{w_2} \rangle}{\langle S \rangle^2} - 1 = -\hat{\Delta}''(w_1 - w_2). \quad (8)$$

Here S_w is the size of an avalanche at w , and $\langle S_w \rangle = \langle S \rangle$. The numerator $\langle S_{w_1} S_{w_2} \rangle$ is the expectation of the product of avalanche sizes, given that one is triggered at $w = w_1$, and a second at $w = w_2$; depends on $|w_1 - w_2|$, and is averaged over the remaining variable. The experimental verification of this relation is shown on Fig. 4. Despite large statis-

tical fluctuations, both the functional form as the amplitude agree. Since $\hat{\Delta}(w)$ is convex, $\hat{\Delta}''(w) \geq 0$. On the other hand, $\langle S_{w_1} S_{w_2} \rangle \geq 0$, thus $\hat{\Delta}''(w) \leq 1$. This bound is impossible to reach, as the toy-model (C6) in $d = 0$ has $\hat{\Delta}''(0^+) = 0.5$. The field theory [8] gives

$$\hat{\Delta}''(0^+) \leq \frac{2}{9} + 0.107533\varepsilon + \mathcal{O}(\varepsilon^2), \quad (9)$$

which evaluates to 0.437 for SR ($\varepsilon = 2$), and 0.222 ($\varepsilon = 0$) for LR correlations. Fig. 4 shows that this bound is saturated, both for the SR and LR sample. This is surprising as both systems have multiple domain walls, estimated to be around five for the samples on Fig. 4. So either all but one domain wall are pinned, or these multiple walls are so highly correlated that they effectively behave as a single wall.

In this paper, we measured the effective force or center-of-mass correlations showing that they have a universal form, predicted by the FRG, both for SR and LR elasticity and mostly independent of ECs. We prove that FRG, an alternative to replica symmetry breaking, correctly models subtle details such as the dependence on dimension and the range of interactions. We hope this work inspires the experimental community to look beyond commonly studied observables and beyond MF. Further experimental systems to explore are sheered colloids or foams, DNA unzipping, and earthquakes.

ACKNOWLEDGMENTS

We thank A. Douin, F. Lechenault, G. Mukerjee and A. Rosso for discussions. F.B. and R.L.S. acknowledge financial support from CNPq and CAPES.

-
- [1] M. Mézard, G. Parisi and M.A. Virasoro, *Spin Glas Theory and Beyond*, World Scientific, Singapore, 1987.
- [2] G. Parisi, *Infinite number of order parameters for spin-glasses*, *Phys. Rev. Lett.* **43** (1979) 1754–1756.
- [3] G. Parisi, *The order parameter for spin glasses: a function on the interval 0-1*, *J. Phys. A* **13** (1980) 1101–1112.
- [4] M. Talagrand, *Mean Field Models for Spin Glasses*, Volume I: *Basic Examples*, Springer Verlag, Berlin, Heidelberg, 2011.
- [5] M. Talagrand, *Mean Field Models for Spin Glasses*, Volume II: *Advanced Replica-Symmetry and Low Temperature*, Springer Verlag, Berlin, Heidelberg, 2011.
- [6] D.S. Fisher, *Interface fluctuations in disordered systems: $5 - \epsilon$ expansion*, *Phys. Rev. Lett.* **56** (1986) 1964–97.
- [7] T. Nattermann, S. Stepanow, L.-H. Tang and H. Leschhorn, *Dynamics of interface depinning in a disordered medium*, *J. Phys. II (France)* **2** (1992) 1483–8.
- [8] K.J. Wiese, *Theory and experiments for disordered elastic manifolds, depinning, avalanches, and sandpiles*, *Rep. Prog. Phys.* **85** (2022) 086502 (133pp), [arXiv:2102.01215](#).
- [9] F. Bohn, G. Durin, M.A. Correa, N.R. Machado, R.D. Della Pace, C. Chesman and R.L. Sommer, *Playing with universality classes of Barkhausen avalanches*, *Scientific Reports* **8** (2018) 11294.
- [10] H. Barkhausen, *Zwei mit Hilfe der neuen Verstärker entdeckte Erscheinungen*, *Phys. Ztschr.* **20** (1919) 401–403.
- [11] J.P. Sethna, K.A. Dahmen and C.R. Myers, *Crackling noise*, *Nature* **410** (2001) 242–250.
- [12] G. Durin and S. Zapperi, *The Barkhausen effect*, in G. Bertotti and I. Mayergoyz, editors, *The Science of Hysteresis*, page 51, Amsterdam, 2006, [cond-mat/0404512](#).
- [13] O. Perkovic, K. Dahmen and J.P. Sethna, *Avalanches, Barkhausen noise, and plain old criticality*, *Phys. Rev. Lett.* **75** (1995) 4528–4531.
- [14] G. Durin and S. Zapperi, *Scaling exponents for Barkhausen avalanches in polycrystalline and amorphous ferromagnets*, *Phys. Rev. Lett.* **84** (2000) 4705–4708.
- [15] S. Zapperi, C. Castellano, F. Colaiori and G. Durin, *Signature of effective mass in crackling-noise asymmetry*, *Nat. Phys.* **1** (2005) 46–49.
- [16] S. Papanikolaou, F. Bohn, R.L. Sommer, G. Durin, S. Zapperi and J.P. Sethna, *Universality beyond power laws and the average avalanche shape*, *Nature Physics* **7** (2011) 316–320.
- [17] L. Laurson, X. Illa, S. Santucci, K.T. Tallakstad, K.J. Måløy and M.J. Alava, *Evolution of the average avalanche shape with the universality class*, *Nat. Commun.* **4** (2013) 2927.
- [18] G. Durin, F. Bohn, M.A. Correa, R.L. Sommer, P. Le Doussal and K.J. Wiese, *Quantitative scaling of magnetic avalanches*, *Phys. Rev. Lett.* **117** (2016) 087201, [arXiv:1601.01331](#).
- [19] B. Alessandro, C. Beatrice, G. Bertotti and A. Montorsi, *Domain-wall dynamics and Barkhausen effect in metallic ferromagnetic materials. I. Theory*, *J. Appl. Phys.* **68** (1990) 2901.
- [20] B. Alessandro, C. Beatrice, G. Bertotti and A. Montorsi, *Domain-wall dynamics and Barkhausen effect in metallic ferromagnetic materials. II. Experiments*, *J. Appl. Phys.* **68** (1990) 2908.
- [21] F. Colaiori, *Exactly solvable model of avalanches dynamics for Barkhausen crackling noise*, *Adv. Phys.* **57** (2008) 287, [arXiv:0902.3173](#).
- [22] D.S. Fisher, *Collective transport in random media: From superconductors to earthquakes*, *Phys. Rep.* **301** (1998) 113–150.
- [23] A. Dobrinevski, P. Le Doussal and K.J. Wiese, *Avalanche shape and exponents beyond mean-field theory*, *EPL* **108** (2014) 66002, [arXiv:1407.7353](#).
- [24] A. Dobrinevski, *Field theory of disordered systems – avalanches of an elastic interface in a random medium*, PhD Thesis, ENS Paris (2013), [arXiv:1312.7156](#).
- [25] P. Le Doussal and K.J. Wiese, *How to measure Functional RG fixed-point functions for dynamics and at depinning*, *EPL* **77** (2007) 66001, [cond-mat/0610525](#).
- [26] O. Narayan and D.S. Fisher, *Threshold critical dynamics of driven interfaces in random media*, *Phys. Rev. B* **48** (1993) 7030–42.
- [27] P. Le Doussal, *Finite temperature Functional RG, droplets and decaying Burgers turbulence*, *Europhys. Lett.* **76** (2006) 457–463, [cond-mat/0605490](#).
- [28] C. ter Burg and K.J. Wiese, *Mean-field theories for depinning and their experimental signatures*, *Phys. Rev. E* **103** (2021) 052114, [arXiv:2010.16372](#).
- [29] See Supplemental Material for details on the samples, the data analysis, error estimates, and the field theory.
- [30] P. Chauve, P. Le Doussal and K.J. Wiese, *Renormalization of pinned elastic systems: How does it work beyond one loop?*, *Phys. Rev. Lett.* **86** (2001) 1785–1788, [cond-mat/0006056](#).
- [31] P. Le Doussal, K.J. Wiese and P. Chauve, *2-loop functional renormalization group analysis of the depinning transition*, *Phys. Rev. B* **66** (2002) 174201, [cond-mat/0205108](#).
- [32] A. Rosso, P. Le Doussal and K.J. Wiese, *Numerical calculation of the functional renormalization group fixed-point functions at the depinning transition*, *Phys. Rev. B* **75** (2007) 220201, [cond-mat/0610821](#).
- [33] P. Le Doussal, K.J. Wiese, S. Moulinet and E. Rolley, *Height fluctuations of a contact line: A direct measurement of the renormalized disorder correlator*, *EPL* **87** (2009) 56001, [arXiv:0904.4156](#).
- [34] K.J. Wiese, M. Bercy, L. Melkonyan and T. Bizebard, *Universal force correlations in an RNA-DNA unzipping experiment*, *Phys. Rev. Research* **2** (2020) 043385, [arXiv:1909.01319](#).
- [35] A.A. Middleton, *Asymptotic uniqueness of the sliding state for charge-density waves*, *Phys. Rev. Lett.* **68** (1992) 670–673.
- [36] P. Le Doussal and K.J. Wiese, *Driven particle in a random landscape: disorder correlator, avalanche distribution and extreme value statistics of records*, *Phys. Rev. E* **79** (2009) 051105, [arXiv:0808.3217](#).
- [37] A. Fedorenko and S. Stepanow, *Depinning transition at the upper critical dimension*, *Phys. Rev. E* **67** (2003) 057104, [cond-mat/0209171](#).
- [38] P. Le Doussal and K.J. Wiese, *Higher correlations, universal distributions and finite size scaling in the field theory of depinning*, *Phys. Rev. E* **68** (2003) 046118, [cond-mat/0301465](#).
- [39] T. Thiery, P. Le Doussal and K.J. Wiese, *Universal correlations between shocks in the ground state of elastic interfaces in disordered media*, *Phys. Rev. E* **94** (2016) 012110, [arXiv:1604.05556](#).
- [40] E.F. Silva, M.A. Corrêa, R.D. Della Pace, C.C. Plá Cid, P.R. Kern, M. Carara, C. Chesman, O. Alves Santos, R.L. Rodríguez-Suárez, A. Azevedo, S.M. Rezende and F. Bohn, *Thickness dependence of the magnetic anisotropy and dynamic magnetic response of ferromagnetic NiFe films*, *J. Phys. D* **50** (2017) 185001.

Supplementary Material for “Force Correlations in Disordered Magnets” by C. ter Burg, F. Bohn, G. Durin, R.L. Sommer, and K.J. Wiese

Appendix A: Samples and experiments

In this work, we analyze force correlations in soft magnetic materials. We employ two thin films and two ribbons to perform our Barkhausen-noise experiments. The thin films consist of an amorphous $\text{Fe}_{75}\text{Si}_{15}\text{B}_{10}$ (FeSiB) film and a polycrystalline $\text{Ni}_{81}\text{Fe}_{19}$ (NiFe) film, both with a thickness of 200 nm. The films are prepared by magnetron sputtering onto glass substrates, with dimensions $10 \text{ mm} \times 4 \text{ mm}$, using the parameters given in Refs. [9]. Detailed information on the structural and magnetic characterizations is provided in Refs. [9, 16, 40]. Our ribbons are an amorphous $\text{Fe}_{64}\text{Co}_{21}\text{B}_{15}$ (FeCoB) and a polycrystalline FeSi alloy with Si=7.8%. Both ribbons have dimensions of about $20 \text{ cm} \times 1 \text{ cm}$, with thickness of $\sim 20 \mu\text{m}$. Further information on the ribbons and their magnetic behavior are given in Refs. [12, 14].

Regarding the Barkhausen experiments, we record noise time series using the traditional inductive technique in an open magnetic circuit, in which one detects voltage pulses with a pickup coil wound around a ferromagnetic material submitted to a smooth, slow-varying external magnetic field. In our setup, sample and pickup coils are inserted in a long solenoid with compensation for the borders to ensure an homogeneous applied magnetic field on the sample. The sample is driven by a triangular magnetic field, applied along the main axis of the sample, with an amplitude high enough to saturate it magnetically. The pickup coil is wound around the central part of the sample. A second pickup coil, with the same cross section and number of turns, is used to compensate the signal induced by the magnetizing field. The Barkhausen signal is then amplified, filtered, and finally digitalized.

For the thin films, the Barkhausen experiments are performed in Brazil. The measurements are carried out using a pickup coil with 400 turns, 3.5 mm long and 4.5 mm wide, and under similar conditions, i.e., 50 mHz triangular magnetic field, 100 kHz 12-dB/octave low-pass filter set in the preamplifier (SR560 Stanford Research Systems) and signal acquisition taken with an analog-to-digital converter board (PCI-DAS4020/12 Measurement Computing) with sampling rate of 4×10^6 samples per second [9]. At a preanalysis stage, we employ a Wiener deconvolution [16], which optimally filters the background noise and removes distortions introduced by the response functions of the measurement apparatus in the original voltage pulses, thus providing reliable statistics despite the reduced intensity of the signal.

For the ribbons, the experiments are performed in Italy. They are carried out using a pickup coil with 50 turns, 1 mm long and 1 cm wide, a triangular magnetic field with frequency between 3-50 mHz, and a low-pass preamplifier filter chosen in the 3-20 kHz range, roughly half of the sampling rate. Specifically, we consider sampling rate of 50×10^3 samples per second for FeCoB, and 20×10^3 samples per second for FeSi [12, 14]. For the FeCoB ribbon, the sample is submitted

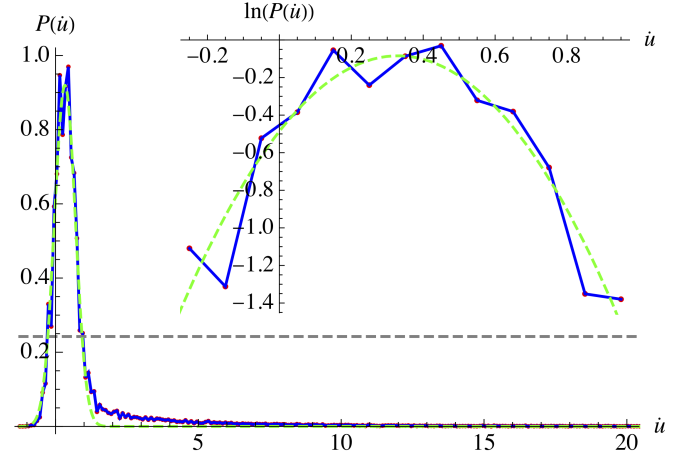


FIG. 5. Distribution $P(\dot{u})$ (blue, solid) with fit (green, dashed) to all data points above the dashed line. It is obtained from the optimal parabolic fit for $\ln P(\dot{u})$, as shown in the inset. The \dot{u} -value at the maximum of the fit is used as the position for the zero of \dot{u} .

to a small tensile stress of 2 MPa during the measurement in order to enhance the signal-to-noise ratio.

All time series for films and ribbons are acquired around the central part of the hysteresis loop, near the coercive field, where the domain wall motion is the main magnetization mechanism and the noise achieves the condition of stationarity [12]. For each experimental run, the statistical properties are obtained from at least 150 measured time series.

While the central issue in this work is to explore the force correlations from the Barkhausen-noise time series, the classification into the different universality classes reposes on earlier work, where we identified the universality class of Barkhausen avalanches by measuring the distributions of avalanche sizes and durations, the average size as a function of the avalanche duration, their power spectrum, and the average avalanche shape. The results for the thin films can be found in Refs. [9, 16], the ones for the ribbons in Refs. [12, 14].

Appendix B: Subtraction of the baseline, measurement of $\hat{\Delta}(w)$, and error estimates

1. Correcting the baseline

Here we present the methods used to obtain the correlator $\hat{\Delta}_v(w)$ defined in Eq. (2) from the experimental data for the change in flux $\dot{u}_{w=vt} \equiv \dot{u}(t)$. As the magnetic field is increased at a rate v

$$u_w - w = \int_0^{w/v} dt [\dot{u}^{\text{raw}}(t) - v]. \quad (\text{B1})$$

We found that there are strong *run-to-run* fluctuations for the mean $v_i := \langle \dot{u}^{\text{raw}} \rangle_i$ in run i , due to a drift in the amplifier baseline. If the estimate for v in (B1) is not correct, this adds a term of the form cw to $u_w - w$, with c a random number. If we suppose that c is Gauss-distributed

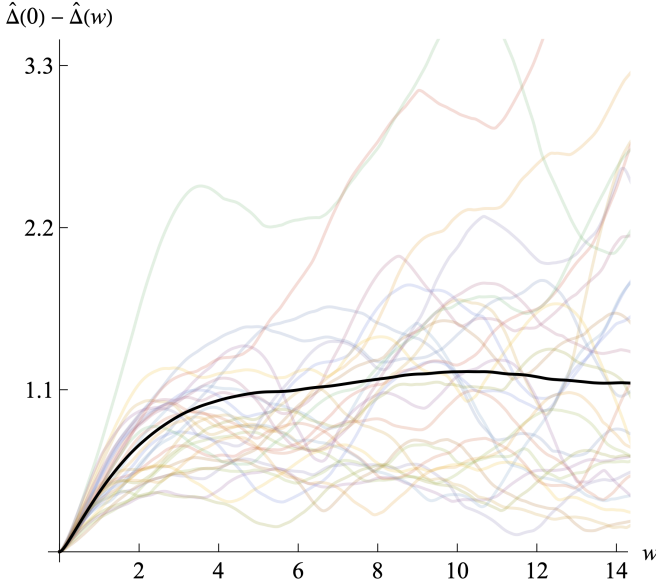


FIG. 6. The correlator $\hat{\Delta}_v(w)$ as given by Eq. (B5) for the FeSiB film (black) with SR elasticity and no ECs. Shaded in the background are the averages \mathcal{M}_i over a single sweep from (B4) which show strong run-to-run fluctuations.

with mean 0, integration leads to a parabolic contribution, i.e. $\hat{\Delta}_v(w) \rightarrow \hat{\Delta}_v(w) + \frac{1}{2} \langle c^2 \rangle w^2$. To correct this, we proceed as follows: For each run i we consider the distribution $P(\dot{u})$ (see Fig. 5), and fit a Gaussian to its peak. This is done by choosing the data points which satisfy $P(\dot{u}) > 0.25 \max_{\dot{u}} P(\dot{u})$, and then fitting a parabola to $\ln[P(\dot{u})]$. Finally, \dot{u} is shifted so that the maximum of the parabola lies at $\dot{u} = 0$. Our best estimate for the driving velocity is then the average over N runs

$$v = \frac{1}{N} \sum_{i=1}^N \langle \dot{u} \rangle_i. \quad (\text{B2})$$

This allows us to construct the interface position $u_w - w$ for run i as

$$u_w^i - w = \int_0^{w/v} dt [\dot{u}_i(t) - v]. \quad (\text{B3})$$

The experimental setup makes appear an additional numerical prefactor on the r.h.s. of Eq. (B3). It is eliminated by demanding that the linearly increasing parts of Fig. 1 have slope 1.

2. Error bars

The connected two-point correlations of the center of mass for run i are

$$\mathcal{M}_i(w - w') := \frac{1}{2} \left\langle [(u_w - w) - (u_{w'} - w')]^2 \right\rangle_i. \quad (\text{B4})$$

Whereas the \mathcal{M}_i show strong fluctuations (see Fig. 6), their mean (black)

$$\hat{\Delta}_v(0) - \hat{\Delta}_v(w) = \frac{1}{N} \sum_{i=1}^N \mathcal{M}_i(w), \quad (\text{B5})$$

is much more stable. Statistically, the small- w region is more robust than the large- w tail.

Given $\mathcal{M}_i(w)$, we need to achieve two goals: (i) extract the plateau height $\hat{\Delta}(0) = \lim_{w \rightarrow \infty} \hat{\Delta}(0) - \hat{\Delta}(w)$ for large w (see Fig. 6), and (ii) estimate the statistical error. Due to the large fluctuations between runs, the distribution of \mathcal{M}_i is not a Gaussian, and standard tools for error analysis fail. The key to solve this problem is to observe that the central limit theorem still applies: partial means over $n < N$ runs have a statistics which increasing n gets closer and closer to that of a Gaussian. As we have always at least $N = 150$ runs, this improvement is substantial, as we can take n up to $n = N/2$. This procedure is known as the *statistical resampling method*: One randomly divides all datasets into two parts and computes the variance of the partial means. Averaging this over 100 random partitions gives a robust estimate for the variance. This is formalized in appendix A of [34]. To obtain the error bars for the shape shown in the main text, all partial means have been rescaled such that their derivative at $w = 0$ equals the mean of $\hat{\Delta}'(0^+)$ over all runs. Only then statistical resampling is applied. This takes out amplitude fluctuations and reduces the error bars to errors of the shape. To summarize, our experiment for given w can be modeled as

$$\hat{\Delta}_{\text{exp}}(w) = \hat{\Delta}(w) + \sigma(w)\eta, \quad (\text{B6})$$

where η is a Gaussian random variable with mean zero and variance 1.

3. Estimate of the total error

In section B2 we obtained error-bars of the shape $\hat{\Delta}(w)$. We still need to put a number on how large the deviations of the measured $\hat{\Delta}(w)$ and the theory are. If Eq. (B6) holds and the (a priori unknown) $\hat{\Delta}(w) = \hat{\Delta}_{\text{th}}(w)$, then we can define a measured η via

$$\eta := \frac{\hat{\Delta}_{\text{exp}}(w) - \hat{\Delta}_{\text{th}}(w)}{\sigma(w)}. \quad (\text{B7})$$

We can turn this into a test: Using η defined by Eq. (B7), it should have variance $\langle \eta^2 \rangle \approx 1$. If we measure a (much) larger $\langle \eta^2 \rangle$, then η has a mean, and theory and experiment do not agree.

The problem of this procedure is that for a given w , we only have one sample. Our statistics can be improved by taking the joint measure for all w . However, the measured values of $\hat{\Delta}(w)$ are correlated, and we cannot simply add up their variances. We propose the following global error estimator

$$\sigma^2 = \frac{1}{\rho} \int_0^{w_{\text{max}}} dw \frac{[\hat{\Delta}_{\text{th}}(w) - \hat{\Delta}_{\text{exp}}(w)]^2}{\sigma(w)^2}. \quad (\text{B8})$$

σ	SR No EC	SR EC	LR No EC	LR EC
1-loop FRG	1.07	1.24	0.28	0.56
2-loop FRG	0.45	0.77	0.76	1.11
$d = 0$	1.89	0.96	2.85	2.03
exponential	3.20	2.95	1.55	3.83

TABLE II. Estimation of σ defined in Eq. (B8) for all combinations of theory and experimental data.

This is best thought of as a discrete sum over all w , divided by the correlation length in the same discretized units. Stated differently, this is the sum of the mean variances per correlation-length segments, equivalent to demanding that the function be satisfied *simultaneously in each* of the w_{\max}/ρ independent segments.

Let us stress that this is the best we can do, and that the variance of the true error may differ by a numerical factor, such as 0.5, 2 or 3. Values for this expression, or more precisely its square root σ are given in table II. One sees that for the SR samples the agreement is best with the resummed 2-loop FRG. For LR samples the best agreement is with the 1-loop FRG. We also see that the measured variances σ^2 for the best matching theory are in general about four times smaller than the next best one. This corroborates our statements made in the main text.

Appendix C: Theory predictions for the different classes

The extracted fixed-point function $\hat{\Delta}(w)$ can be compared to results from the functional renormalization group (FRG) sketched below. As we cannot give more than a short summary here, we refer to sections 2 and 3 of the recent review [8] for a pedagogic introduction.

Contrary to conventional RG, where one considers the flow of a single coupling constant, the FRG follows the flow of an entire function, here the disorder-force correlator $\Delta(w)$ introduced in Eq. (2). Writing $\varepsilon = d_c - d$ for the expansion parameter around the upper critical dimension d_c , the FRG fixed-point equation for the rescaled (dimensionless) correlator $\tilde{\Delta}(w)$ reads at 1-loop order (leading order in ε)

$$\partial_t \tilde{\Delta}(w) = (\varepsilon - 2\zeta) \tilde{\Delta}(w) + \zeta u \tilde{\Delta}'(w) - \frac{d^2}{dw^2} \frac{1}{2} [\tilde{\Delta}(w) - \tilde{\Delta}(0)]^2 + \dots \quad (\text{C1})$$

with the dots representing higher-order contributions [30, 31] in an expansion in ε . This equation has solutions which decay at least exponentially fast only for selected values of the roughness exponent ζ . For the RF disorder present in the experiment, the appropriate solution of the fixed-point equation $\partial_t \tilde{\Delta}(w) = 0$ associated to Eq. (C1) is (see e.g. Ref. [8])

$$\tilde{\Delta}^{1\text{-loop}}(w) = -\frac{\varepsilon}{3} W\left(-\exp\left(-\frac{w^2}{2} - 1\right)\right) + \mathcal{O}(\varepsilon^2), \quad (\text{C2})$$

$$\zeta = \frac{\varepsilon}{3} + \mathcal{O}(\varepsilon^2). \quad (\text{C3})$$

Here $W(z)$ is the product-log function, the principle solution for x in $z = xe^x$. The observable in Eq. (2) is obtained from

$\hat{\Delta}(w)$	$\frac{\hat{\Delta}(0)\hat{\Delta}''(0)}{\hat{\Delta}'(0^+)^2}$	$\hat{\Delta}''(0)$
Exponential	1	1
$d = 0$, Eq. (C6)	0.822	$\frac{1}{2}$
2-loop FRG for $d = 2$ (SR)	0.75	≤ 0.437
1-loop FRG, Eq. (C2) (LR)	$\frac{2}{3}$	$\leq \frac{2}{9}$
SR elasticity without ECs	0.73(3)	0.37(2)
SR elasticity with ECs	0.65(10)	0.41(2)
LR elasticity without ECs	0.58(10)	0.17(5)
LR elasticity with ECs	0.65(10)	0.24(4)

TABLE III. Comparison of theoretically and experimentally obtained amplitudes and amplitude ratios. Theory values are obtained by Taylor-expanding Eqs. (C2) (1-loop) and (C6) ($d = 0$). The 2-loop results can be found in [8, 31].

the (scale-free) fixed-point solution $\tilde{\Delta}(w)$ as

$$\hat{\Delta}(w) = \mathcal{A} \hat{\rho}^2 \tilde{\Delta}(w/\hat{\rho}), \quad (\text{C4})$$

$$\hat{\rho} := \rho \frac{|\tilde{\Delta}'(0)|}{\tilde{\Delta}(0)}. \quad (\text{C5})$$

The amplitude \mathcal{A} is a number (depending on mL), whereas the correlation length ρ of Eqs. (C7) and (C4) scales as $\rho \sim m^{-\zeta}$. The fixed point (C2)-(C3) gets corrected at 2-loop order [30, 31] as more terms appear in Eq. (C1). In principle, it allows us to predict $\hat{\Delta}(w)$ for domain-wall dimensions between $d = 4$ down to $d = 0$. The bulk magnets used here have $d = 2$ ($\varepsilon = 2$), whereas a thin magnetic film has $d = 1$ ($\varepsilon = 3$). Dimension $d = 0$ ($\varepsilon = 4$) is realized in the DNA/RNA peeling experiment of Ref. [34]. The precision of the approximation decreases with d , since the expansion parameter $\varepsilon = 4 - d$ increases. We are in the fortunate position to have an analytic solution in $d = 0$ [28, 36],

$$\hat{\Delta}^{d=0}(w) = \frac{w^2}{2} + \text{Li}_2(1 - e^w) + \frac{\pi^2}{6}. \quad (\text{C6})$$

This allows us to choose a Padé approximant for the 2-loop result, optimized for agreement with the solution (C6). A summary of properties for $\hat{\Delta}(w)$ for the different classes is presented in table III.

In the experiment, each function contains two scales, the amplitude $\hat{\Delta}(0)$ and a correlation length ρ in the w -direction. The latter is defined by

$$\rho := \frac{\hat{\Delta}(0)}{|\hat{\Delta}'(0^+)|}. \quad (\text{C7})$$

It enters into the scaling form (C4) as indicated. Rescaling the theory candidates to have the same $\hat{\Delta}(0)$ and $\hat{\Delta}'(0^+)$ ensures that one compares the shape without any fitting parameter. This is the form used in the main text.

Finally let us mention that the normalization in Eq. (2) is different from the one used in the field theory [25], which contains an additional factor of $m^4 L^d$, with L the system size, on the r.h.s. Our choice is motivated by a lack in the knowledge of m^2 and L , and by the reduction of scales in $\hat{\Delta}_v(w)$ to a single one, namely the correlation length $\rho := \hat{\Delta}(0)/\hat{\Delta}'(0^+)$ in the w -direction.

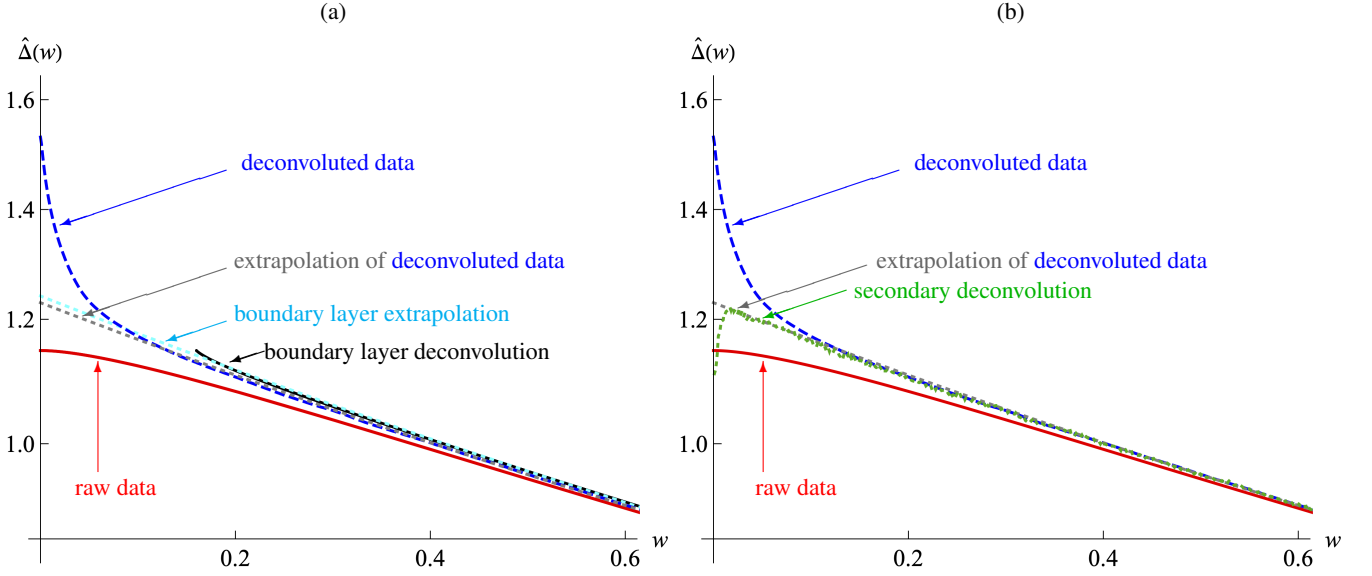


FIG. 7. Comparison of three different deconvolution procedure for the 200-nm-thick FeSiB film with SR elasticity and no ECs (raw data in solid, red): deconvolution via Eq. (D7) as discussed in the main text (blue dashed), time scale $\tau = 0.175$, and extrapolation (grey, dotted). In (a) is shown in addition deconvolution via the boundary layer given by Eqs. (D7)-(D8) (black, solid) using the same $\tau = 0.175$, and its extrapolation (cyan, dotted). In (b) is shown the result of secondary deconvolution using Eq. (E1) (green, dotted), with $\tau = 0.175$ and $\tau' = 0.0024$.

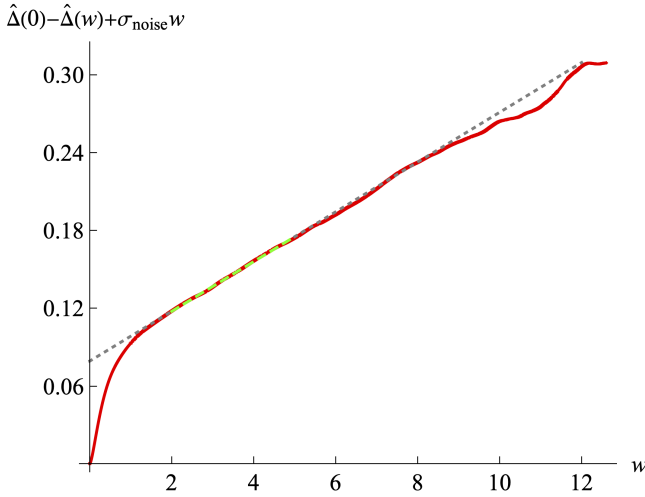


FIG. 8. Subtraction of a linear noise contribution (grey dotted, fitting region in green dashed) $\Delta(0) + \sigma_{\text{noise}}|w|$ for the FeCoB ribbon with SR elasticity and ECs at $v = 2$.

Appendix D: Deconvolution of $\hat{\Delta}_v(w)$.

Suppose the response function decays exponentially with time scale τ ,

$$R(t) = \frac{1}{\tau} e^{-t/\tau} \Theta(t). \quad (\text{D1})$$

Then it satisfies the differential equation

$$(1 + \tau \partial_t) R(t) = \delta(t), \quad (\text{D2})$$

and is normalized,

$$\int_0^\infty R(t) dt = 1. \quad (\text{D3})$$

This allows us to invert Eq. (4) as [28]

$$\begin{aligned} \hat{\Delta}(w) &= (1 + v\tau \partial_w)(1 - v\tau \partial_w) \hat{\Delta}_v(w) \\ &= (1 - (v\tau)^2 \partial_w^2) \hat{\Delta}_v(w). \end{aligned} \quad (\text{D4})$$

Taking derivatives of the measured function $\hat{\Delta}_v(w)$ is noisy, but we are in the fortunate position to have direct access to the velocity correlation function $\hat{\Delta}_{\dot{u}}(w)$,

$$\hat{\Delta}_{\dot{u}}(w - w') := \overline{\dot{u}_w \dot{u}_{w'}} = -v^2 \hat{\Delta}_v''(w - w'). \quad (\text{D5})$$

Using this in Eq. (D4) we get Eq. (5) of the main text,

$$\hat{\Delta}(w) = \hat{\Delta}_v(w) + \tau^2 \hat{\Delta}_{\dot{u}}(w). \quad (\text{D6})$$

In the small- v limit Eq. (4) can be approximated by a boundary-layer ansatz [8, 28], which gives an alternative, robust, albeit less precise, deconvolution procedure,

$$\hat{\Delta}_v(w) = \hat{\Delta}(\tilde{w}), \quad (\text{D7})$$

$$\tilde{w} := \sqrt{w^2 + (v\tau)^2}. \quad (\text{D8})$$

Our second strategy to reconstruct $\hat{\Delta}(w)$ is to plot $\hat{\Delta}_v(w)$ vs. \tilde{w} , and determine τ which gives the straightest curve at small \tilde{w} . An example is shown in Fig. 7(a).

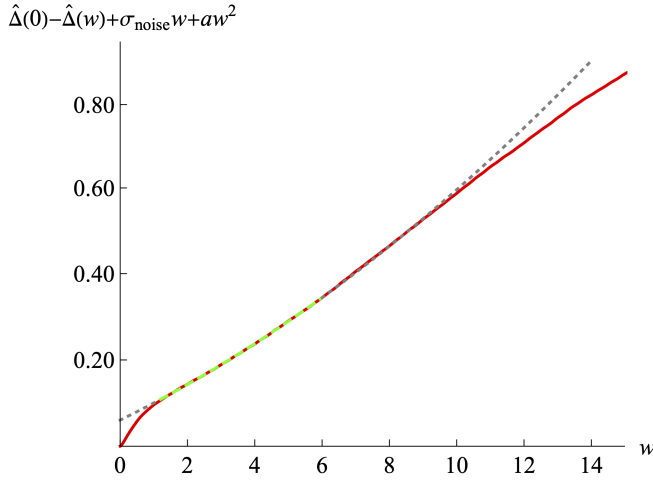


FIG. 9. Subtraction of the noise contribution $\hat{\Delta}(0) + \sigma_{\text{noise}}|w| + aw^2$ with a small parabolic contribution (grey dotted, fitting region in green dashed) for the FeSi ribbon with LR elasticity and ECs at $v = 1$. The parabolic term with $a \geq 0$ results from small errors in the procedure of App. B to estimate the baseline of \dot{u}_w .

Appendix E: Higher-order deconvolution

We showed that application of Eq. (D6) to the measured $\hat{\Delta}_v(w)$ removes part of the boundary layer $\delta_w = v\tau$, but that it creates a new smaller boundary layer of size δ'_w . On a phenomenological level, we found that inclusion of an additional term substantially improves the accuracy,

$$\hat{\Delta}(w) = \hat{\Delta}_v(w) + \tau^2 [1 + v\tau' \partial_w + \dots] \hat{\Delta}_{\dot{u}}(w). \quad (\text{E1})$$

Such a term may arise for a non-exponentially decaying response function $R(t)$. In principle, the procedure can be improved using a second-order derivative in the square brackets. While a single derivative of $\hat{\Delta}_{\dot{u}}(w)$ still gives a signal relatively free of noise, adding a second derivative is not possible for our data. In Fig. 7(b) we show for the FeSiB film the result of the deconvolution (D6) compared to the improved deconvolution (E1).

Appendix F: Details for the four samples

1. FeSiB film: SR interactions without ECs

For the amorphous FeSiB film with thickness of 200 nm, we show in Fig. 6 the means \mathcal{M}_i for a single run (in color), compared to the mean $N^{-1} \sum_{i=1}^N \mathcal{M}_i$ over all N runs (in black).

$\hat{\Delta}_v(0)$ is extracted from the plateau value at large w . Subtracting $\hat{\Delta}_v(0)$ gives the curve reported in the main text in Fig. 2. In Fig. 7 we show for the same sample comparison of deconvolution via Eq. (5) discussed in the main text, deconvolution via the boundary layer (D7)-(D8) and secondary deconvolution via Eq. (E1). All procedures are in quantitative agreement. In our chosen units, $w = 1$ corresponds to 2.5 ms, assuming a single wall to estimate the driving velocity. Due to the high level of correlation between the walls, we believe this estimation is justified. The number of domain walls is estimated to be around 3000 [9]. This implies that $w = 1$ corresponds to approximately 1.5 mm.

2. FeCoB ribbon: SR interactions with ECs

For the amorphous FeCoB ribbon, Fig. 8 shows the subtraction of $\hat{\Delta}(0)$ plus an additional linear contribution due to white noise as given in Eq. (7). All data presented in the main text are after this subtraction. In our chosen units, $w = 1$ corresponds to $0.2 \text{ s} \approx 135 \mu\text{m}$. The number of domain walls is estimated to be around 5.

3. NiFe film: LR interactions without ECs

deconvolution as presented in Fig. 3(a) for the polycrystalline NiFe film having thickness of 200 nm is done using $\tau = 0.39$. In our chosen units, $w = 1$ corresponds to $2.5 \text{ ms} \approx 100 \mu\text{m}$. The number of domain walls is estimated to be around 5000 [40].

4. FeSi ribbon: LR interactions with ECs

Fig. 9 shows the subtraction of a linear term plus a small parabolic contribution for the polycrystalline FeSi ribbon. The latter parabolic contribution arises if our estimate for the baseline of \dot{u} for run i still contains a small error, see the discussion after Eq. (B1). The deconvolution shown in the main text in Fig. 3(a) has been done using $\tau = 0.055$. In our chosen units, $w = 1$ corresponds to $50 \text{ ms} \approx 1.385 \mu\text{m}$. The number of domain walls is estimated to be around 5.

Appendix G: Velocity correlations $\hat{\Delta}_{\dot{u}}(w)$

Measurements of the velocity correlations $\hat{\Delta}_{\dot{u}}(w)$ for our samples are shown in Fig. 10. The scale on which $\hat{\Delta}_{\dot{u}}(w)$ decays to zero is the same as the correlation length ρ of $\hat{\Delta}(w)$ defined in Eq. (C7).

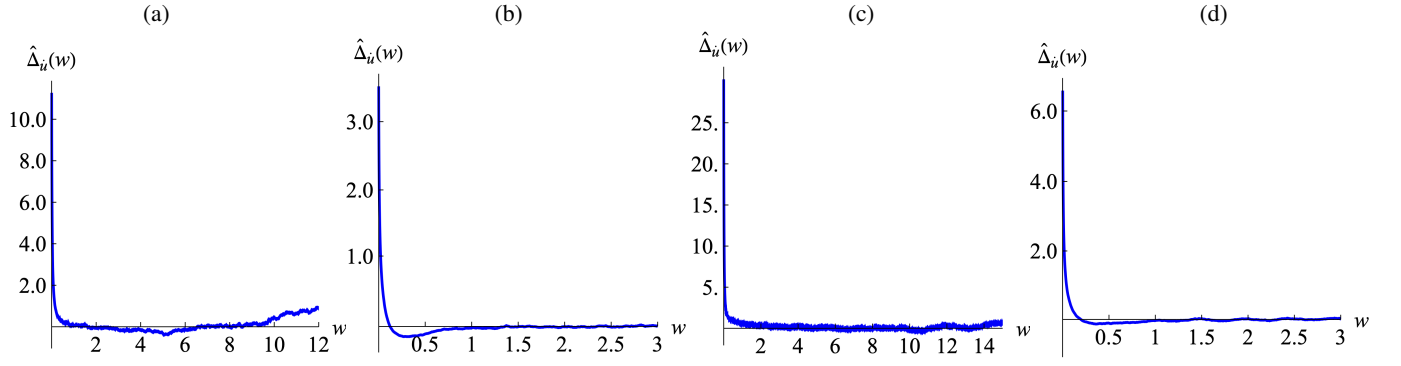


FIG. 10. The correlation function $\hat{\Delta}_u(w)$ of the domain wall velocity \dot{u} . The scale on which $\hat{\Delta}_u(w)$ decays to 0 is the correlation length ρ of $\hat{\Delta}(w)$. Plots are ordered, as in the main text, for **(a)** FeSiB film (SR elasticity, no ECs). **(b)** FeCoB ribbon (SR elasticity, ECs). **(c)** NiFe film (LR elasticity, no ECs). **(d)** FeSi ribbon (LR elasticity, ECs).